Journal of
Materials Chemistry A

Materials for energy and sustainability

Accepted Manuscript

This article can be cited before page numbers have been issued, to do this please use: Y. Shi, S. Li, Y. Li, X. Wang, J. Zhang, L. Zhao, J. Xu, Y. Wang, H. Ren, W. Xing and G. zhao, *J. Mater. Chem. A*, 2025, DOI: 10.1039/D5TA04475H.

ROYAL SOCIETY OF CHEMISTRY

rsc.li/materials-a

View Article Online
DOI: 10.1039/D5TA04475H

View Article Online
DOI: 10.1039/D5TA04475H

Computational design of Nb-Mo dual sites on $MoSe_2$ edges for synergistic urea electrosynthesis

Jing Xu,[a] Ye Shi,[a] Yizhu Wang,[a] Shouao Li,[a] Yuan Li,[a] Xueru Wang,[a] Jinghao Zhang,[a] Hao Ren,[a] Wei Xing,[a] Guang Zhao,[b] and Lianming Zhao*[a]

[a] Shandong Key Laboratory of Intelligent Energy Materials, School of Materials Science and Engineering, China University of Petroleum (East China), Qingdao, Shandong 266580, China

[b] School of Petroleum Engineering, China University of Petroleum (East China), Qingdao, Shandong 266580, China

*Corresponding authors.

E-mail addresses: lmzhao@upc.edu.cn (L. Zhao).

Abstract

Electrochemical synthesis of urea offers a sustainable alternative to conventional industrial processes as a green synthesis strategy. However, challenges remain in activating inert N_2 molecules and the crucial C-N coupling process. In this work, we doped 3d-5d transition metal atoms at the edge of 2H-$MoSe_2$ (TM-$MoSe_2$) to form Mo-TM bimetallic active sites and explored their potential for urea electrosynthesis from N_2 and CO by density-functional theory calculations. Based on catalyst stability, N_2 adsorption, C-N coupling, and limiting potentials, Ti-, Zr-, Nb-, and Hf-doped $MoSe_2$ catalysts are identified as high-potential electrocatalysts for urea synthesis. Notably, Nb-$MoSe_2$ demonstrates remarkable catalytic performance for urea electrosynthesis, characterized by its exceptional stability, ultralow limiting potential (U_L = −0.35 V),

View Article Online
DOI: 10.1039/D5TA04475H

small kinetic barrier (0.64 eV), and significant suppression of side reactions. Mechanism investigations reveal that the catalytic activity (U_L) of TM-$MoSe_2$ catalysts in urea synthesis exhibits a volcano-shaped relationship with the binding strength of *NCON (ΔG_{*NCON}). Furthermore, the variation of ΔG_{*NCON} is linearly correlated with the bond lengths of adsorbed $^*N_2$ molecules. The high activity of Nb-$MoSe_2$ stems from the effective activation of $^*N_2$ by the synergistic effect of Nb and Mo. This study provides theoretical support for the superior performance of Nb-$MoSe_2$ catalysts in urea electrosynthesis and opens up new perspectives on the potential of transition metal dichalcogenides in electrocatalysis.

1. Introduction

Over the past century, nitrogen fertilizers have profoundly transformed agricultural practices, playing a pivotal role in sustaining global food security and supporting the livelihoods of billions worldwide.[1] As the predominant nitrogen fertilizer, urea stands out for its exceptional nitrogen density (46%) and facile conversion to bioavailable ammonia (NH_3), attributes that have revolutionized modern agrochemical systems and driven unprecedented productivity gains in crop cultivation.[2] Beyond agriculture, urea finds broad applications including pharmaceuticals, textiles, and fuel cell technologies.[3–5] Industrially, urea synthesis primarily relies on the reaction between NH_3 and CO_2 under harsh conditions of elevated temperature and pressure (150–200 °C and 150–250 bar).[6] Approximately 80% of the global ammonia is used in this process for urea production, primarily sourced from the conventional Haber-Bosch method. This process heavily depends on fossil fuels, such as natural gas and coal as energy

View Article Online
DOI: 10.1039/D5TA04475H

sources, resulting in large amounts of CO_2 emissions that account for about 1–2% of global CO_2 emissions.[1,7] Consequently, developing urea synthesis technologies under environmentally benign conditions is critical to reducing fossil fuel dependence and ensuring the sustainable development of human society.

Electrochemical C-N coupling for urea synthesis under ambient conditions has emerged as a promising alternative to traditional methods.[8,9] For example, Chen *et al.*[9] demonstrated $PdCu/TiO_2$ for electrochemical urea synthesis from N_2 and CO_2, yielding 3.36 mmol h^{-1} g^{-1} with 8.92% Faraday efficiency (FE) under ambient conditions. Ma *et al.*[10] designed CeO_2/Co_3O_4 heterostructures, achieving 5.81 mmol h^{-1} g^{-1} urea at −0.2 V and 30.05% FE. Zhao *et al.*[11] developed CoN_3-CoAC/NC catalysts, delivering 20.83 mmol h^{-1} g^{-1} urea at −0.4 V (FE: 23.73%). Theoretically, Zhang *et al.*[12] computationally proposed $Cr_3@C_2N$, enabling urea synthesis at −0.72 V via enhanced N_2/CO_2 co-activation. Liu *et al.*[13] engineered dual-atom $ReV@C_2N$, achieving urea formation at a lower limiting potential (−0.69 V). Jiao *et al.*[14] employed density functional theory (DFT) calculations to investigate a two-dimensional Mo_2P monolayer catalyst for electrocatalytic urea synthesis. Their computational study predicted a low kinetic barrier (0.35 eV) for C–N coupling formation and a low limiting potential (−0.39 V), along with significant suppression of competitive side reactions, indicating excellent catalytic activity. Furthermore, Jiao *et al.*[15] adopted a combined theoretical-experimental approach to characterize the MoP(101) surface. On this catalyst, N_2 and CO_2 were efficiently co-reduced to urea at a low limiting potential (−0.27 V) while maintaining effective suppression of parasitic reactions. The experimental validation

View Article Online
DOI: 10.1039/D5TA04475H

confirmed the theoretical predictions, achieving a urea formation rate of 12.4 μg h^{-1} mg^{-1} and a Faradaic efficiency of 36.5%. Both theoretical and experimental studies confirm the Langmuir-Hinshelwood (LH) mechanism for urea electrosynthesis, where $^{*}CO_2$ is first reduced to $^{*}CO$, followed by desorption and insertion of the side-adsorbed $^{*}N_2$ for coupling, and subsequent hydrogenation to form urea.[16,17]

Despite the remarkable progress made in electrocatalytic urea synthesis in recent years, the electrochemical co-reduction of N_2 and CO_2 still faces many challenges, notably in achieving high product selectivity toward urea. The inherent complexity of N_2 and CO_2 reduction pathways arises from competing side reactions—nitrogen reduction (NRR), CO_2 reduction (CO_2RR), and hydrogen evolution (HER)—which disrupt the desired C-N coupling dynamics.[18] These parasitic processes severely compromise reaction selectivity, manifesting as erratic product distributions and suppressed urea yields. Therefore, strategic suppression of competing pathways coupled with precise steering of C-N bond formation has become a pivotal challenge in advancing electrocatalytic urea synthesis. To address these challenges, researchers have proposed to utilize CO instead of CO_2 as the source of carbonyls in urea synthesis.[19,20] This method simplifies the reaction pathway and enhances selectivity for C-N coupling reactions, significantly improving the efficiency of urea synthesis. Furthermore, CO, as a toxic gas, has long been one of the main components of atmospheric pollution.[21] Thus, utilizing CO as a feedstock for urea synthesis can effectively utilize this exhaust gas, mitigating its negative impact on the environment and human health. The synthesis of urea using N_2 and CO also faces a challenge: The coupling of $^{*}CO$ and $^{*}N_2$ to generate

View Article Online
DOI: 10.1039/D5TA04475H

the urea precursor *NCON is kinetically sluggish and faces a high kinetic barrier, resulting in a low activity.[13,22] The root of this problem is that *CO and $^*N_2$ are typically adsorbed separately at different sites on the catalyst surface. The process of inserting *CO into the $^*N_2$ molecule requires overcoming the strong N≡N bond energy and breaking the N≡N bond, which is a very difficult task.[23,24] Driven by this fundamental challenge, Kong *et al.*[25] systematically investigated single-atom catalysts (SACs) supported on porous boron nitride (p-BN) and proposed an Eley-Rideal (ER) mechanism for the C-N coupling. In the ER mechanism, free CO molecules are directly inserted into the side-adsorbed $^*N_2$ molecules on catalyst surfaces to form a tower-like *NCON key intermediate, which significantly reduces the kinetic barrier of the C-N coupling. Building on the ER mechanism, Zhu *et al.*[19] developed dual-atom catalysts ($M_2@N_6G$ and $MM'@N_6G$) on N-doped graphene substrates. Among 72 screened systems, eight candidates (i.e., $Co_2@N_6G$, $ScNi@N_6G$, $MnFe@N_6G$, $FeNi@N_6G$, $CoNi@N_6G$, $CoRh@N_6G$, $RuRh@N_6G$, $RhNi@N_6G$) were selected out due to their low Gibbs free energy (< 1.0 V) and moderate C-N coupling barriers (1.18–1.62 eV). Zhong *et al.*[26] designed dual-metals anchored on Ti_2CO_2 MXene ($M_2@Ti_2CO_2$ and $MM'@Ti_2CO_2$). The $VMn@Ti_2CO_2$ system were found to exhibit ultra-low limiting potential (−0.26 V) and significant inhibition of competitive reactions (NRR/HER). All these studies indicate that the dispersed bimetallic atoms can serve as effective active sites to promote urea electrosynthesis under the ER mechanism.

In recent years, transition metal dichalcogenides (TMDs) are widely studied for their catalytic activity and unique electronic properties.[27–29] $MoSe_2$ outperforms MoS_2 in

View Article Online
DOI: 10.1039/D5TA04475H

electrocatalysis due to enhanced metallic conductivity, expanded interlayer spacing, and robust stability. First, $MoSe_2$ exhibits intrinsic metallic conductivity originating from the metallic behavior of Se atoms, whose electronic conductivity (1×10^{-3} S m^{-1}) is orders of magnitude higher than sulfur (5×10^{-28} S m^{-1}).[30,31] Second, the expanded interlayer spacing of $MoSe_2$ (~0.65 nm vs. MoS_2: ~0.62 nm) and the larger ionic radius of Se^- (1.98 Å vs. S^{2-}: 1.84 Å) enhance ion diffusion kinetics, reducing mass transport limitations.[32,33] Finally, $MoSe_2$'s broad pH adaptability (0–14), attributed to the strong Se-O bond (~314 kJ mol^{-1}), allows stable operation in diverse environments.[34] $MoSe_2$ crystallizes in two distinct phases dictated by selenium atom arrangement: the thermodynamically stable 2H phase and the metastable 1T phase.[35] While the 2H phase dominates under equilibrium conditions due to its lower formation energy, its basal planes exhibit limited catalytic activity owing to sparse electronic states near the Fermi level and unfavorable adsorbate binding thermodynamics.[36] Consequently, catalytic activity in pristine 2H-$MoSe_2$ primarily localizes at edge sites where undercoordinated Mo atoms serve as active centers.[37,38] Jain *et al.*[37] computationally demonstrated that introducing Se vacancies and edge-site metal doping (e.g., Fe, Co) effectively modulates the d-band center position, enhancing the edge reactivity. Experimental validations by Gao *et al.*[39] and Kuraganti *et al.*[40] revealed that B and Mn-doping can significantly enhance the catalytic performance of the $MoSe_2$ edges. Jiang *et al.*[41] engineered Cu-doped $MoSe_2$ edges with synergistic Cu-Mo dual sites, facilitating cooperative CO_2/NO_3^- adsorption that reduces the C-N coupling barrier from 1.45 eV to 0.68 eV.

View Article Online
DOI: 10.1039/D5TA04475H

In this work, we engineered Mo-TM bimetallic active sites through Se-vacancy-mediated edge reconstruction and 3d–5d transition metal doping in 2H-$MoSe_2$, systematically evaluating their electrocatalytic performance for urea synthesis from N_2 and CO. Following initial stability assessments of edge configurations, the optimal Nb-$MoSe_2$ system is identified through the combined analyses of N_2 adsorption geometry, C-N coupling feasibility, urea selectivity, and limiting potential. The urea synthesis activity of TM-$MoSe_2$ exhibits a volcano-type dependence on *NCON adsorption free energy (ΔG_{*NCON}), which is linearly governed by the bond elongation of $^*N_2$ species ($d_{N\equiv N}$). Ab initio molecular dynamics (AIMD) simulations further confirm thermal robustness, validating practical catalytic viability.

2. Computational method details

All DFT calculations and AIMD simulations were conducted employing the Perdew-Burke-Ernzerhof (PBE) exchange-correlation functional within the generalized gradient approximation (GGA) framework, as implemented in the DMol^3 module.[42,43] The GGA-PBE methodology demonstrates remarkable reliability in reproducing experimental electronic structures and exciton binding energies of MoX_2 (X = S, Se, Te), as evidenced by comparative studies by Komsa and Krasheninnikov.[44] Furthermore, Barja *et al.*[45] revealed excellent agreement between PBE-derived local density of states (LDOS) for monolayer $MoSe_2$ and experimental scanning tunneling spectroscopy measurements, including charge density distribution matching. Notably, the PBE functional has been widely adopted for probing structure-activity correlations between electronic configurations and electrochemical performance in TMDs,

View Article Online
DOI: 10.1039/D5TA04475H

establishing its validity for mechanistic investigations in electrocatalytic systems.[46,47] The PBE method with Hubbard U correction (DFT+U) provides a more accurate description of partially occupied d-orbitals in transition metal atoms.[48] To validate our approach, we performed DFT+U calculations on the representative Nb-$MoSe_2$ catalyst. The results show energetic trends for urea synthesis consistent with those obtained using standard GGA-PBE, with an average deviation of only 0.09 eV (see Fig. S1). Thus, given this consistency, the GGA-PBE method remains sufficient for the present study, and DFT+U was not employed.

To account for long-range dispersion effects, the DFT-D3 method developed by Grimme was employed in this study.[49] The Grimme DFT-D3 method is explicitly parameterized for all 94 elements from H to Pu, which include 5d metals.[49] For validation, we performed comparative calculations on the Hf-$MoSe_2$ catalyst (containing 4d/5d metals) using both Grimme and TS methods. The results show consistent energetic trends for urea synthesis, with an average deviation of only 0.04 eV (Fig. S2), confirming the robustness of our approach. This consistency is further supported by successful applications of Grimme's method to 5d-metal catalysts in prior studies.[50–52]

Electron-ion core interactions were described using density functional semicore pseudopotentials (DSPP), while the double numerical plus polarization (DNP) basis sets were augmented with polarization functions.[53,54] Upon the convergence tests (see Fig. S3), a $6 \times 6 \times 1$ Monkhorst-Pack k-point grid was employed for Brillouin zone sampling, with a global orbital cutoff radius of 5.0 Å set in real space. During geometry

View Article Online
DOI: 10.1039/D5TA04475H

optimization, the following convergence criteria were applied: energy $\leq 1\times10^{-5}$ Ha, max force $\leq 2\times10^{-3}$ Ha/Bohr, max displacement $\leq 5\times10^{-3}$ Bohr. In this study, the involved transition states and dynamical barriers were analyzed by the linear synchronous transit (LST) and quadratic synchronous transition (QST) methods.[55] Finally, AIMD simulations were carried out using the NVT ensemble[56] to assess the thermal stability of the material. For the AIMD simulations, the temperature was set to 300 K and 500 K, respectively, and the time step was set to 2 fs with a total period of 10 ps.

Previous studies have demonstrated that chalcogen vacancy defects are ubiquitous in layered TMDs.[37] These defects can not only be generated spontaneously during synthesis, but also artificially introduced by post-synthesis processing techniques such as ion/electron irradiation, annealing, or plasma treatment.[37] The $(10\bar{1}0)$ edge of $MoSe_2$ has been identified as a structurally stable edge that serves as an active site for catalytic reactions.[57] Therefore, we constructed a 4 × 5 × 1 2H-$MoSe_2$ supercell in which the atoms in the bottom four atomic layers of the supercell were fixed in the calculated lattice positions and the upper five layers were completely relaxed. The cell parameters of 2H-$MoSe_2$ were determined by DFT calculations to be a = 3.296 Å and c = 12.924 Å, with a Mo-Se bond length of 2.543 Å, which are in good agreement with the experimentally measured values (a = 3.288 Å, c = 12.900 Å, Mo-Se = 2.54 Å) (see Table S1).[37,38] A 20.0 Å vacuum layer in the x and z directions was constructed to avoid the interaction of neighboring cells. A vacuum layer of 20.0 Å and 10 Å was constructed in the b and c directions, respectively, to avoid interactions between neighboring cells.

View Article Online
DOI: 10.1039/D5TA04475H

The monolayer TM-$MoSe_2$ model was designed by first generating Se vacancies at edges to activate Mo sites, then substituting edge Mo atoms with isolated 3d–5d transition metals (see Fig. 1a).

The adsorption energy (ΔE) was calculated by the following equation:

$$\Delta E = E_{\text{absorbate/substrate}} - (E_{\text{substrate}} + E_{\text{absorbate}}) \quad (1)$$

where $E_{\text{absorbate/substrate}}$, $E_{\text{substrate}}$, and $E_{\text{absorbate}}$ correspond to the total energy of adsorbate adsorbed on TM-$MoSe_2$ substrates, the energy of the TM-$MoSe_2$ substrate, and the energy of isolated adsorbates, respectively.

The computational hydrogen electrode (CHE) model proposed by Nørskov *et al.* was used to explain the Gibbs free energy change (ΔG) in urea electrosynthesis.[58,59] For the transfer of proton-electron pairs, the Gibbs free energy change was defined as half of the gaseous hydrogen:

$$\Delta G(\mathrm{H^+ + e^-}) = 1/2\Delta G(\mathrm{H_2}) - eU \quad (2)$$

For N_2/CO reduction reactions, the ΔG in each elementary step was calculated by the following equation:

$$\Delta G = \Delta E + \Delta ZPE - T\Delta S \quad (3)$$

where ΔE is the adsorption energy calculated by DFT. ΔZPE and ΔS denote the change in zero-point energy and entropy before and after adsorption, respectively. The $-T\Delta S$ is based on the entropy correction at 298.15 K temperature.[60,61]

To evaluate the catalytic activity of the urea electrosynthesis, the limiting potential (U_L) can be calculated by the following equation:

$$U_L = -\Delta G_{\max}/e \quad (4)$$

View Article Online
DOI: 10.1039/D5TA04475H

where ΔG_{max} is the maximum value of the Gibbs free energy change in the elementary reaction. In addition, e is the transferred charge. A smaller ΔG_{max} correlates with a less negative U_L, implying reduced energy input requirements and consequently enhanced catalytic activity for the urea electrosynthesis.[14]

3. Results and discussion

3.1 Structure and stability of TM-$MoSe_2$

In this work, we designed 22 TM-doped $MoSe_2$ systems by substituting edge Mo atoms with 3d-5d transition metals (TMs), forming Mo-TM dual-active sites (Fig. 1a). The selected TMs spanned 22 elements across the 3d (Ti-Cu), 4d (Zr-Ag), and 5d (Ha-Au) series, excluding the native Mo and radioactive Tc. Each dual-active site comprises a tetracoordinated Mo center and a tetracoordinated TM center bridged by two *ortho*-Se atoms, creating a shared electronic environment for synergistic catalysis. After geometry optimization, some TM-$MoSe_2$ catalysts exhibit a slight structural deformation (Fig. S4 and Table S2), due to the difference in atomic radii of the doped metals. Compared to undoped $MoSe_2$, the systems doped with Zr, Nb, Ag, Hf, Ta, and Au show elongated TM-Se bonds, due their larger atomic radii. In contrast, doping with V, Cr, Mn, Fe, Co, Ni, Cu, Ru, Rh, Pd, Os, Ir, and Pt results in bond contraction, which can be attributed to the smaller atomic radii of these transition metals.

The Hirshfeld charge analysis shows that the bimetallic active sites are positively charged, whereas the neighboring Se atoms are negatively charged (Table S3). As shown in Fig. 1b, a linear correlation exists between the average charge of bimetallic active sites and their adjacent *ortho*-Se atoms, demonstrating direct electron donation

View Article Online
DOI: 10.1039/D5TA04475H

from Mo-TM centers to Se ligands. Therefore, the electronic structure of the active center can be effectively regulated by TM doping, which in turn enhances the catalytic performance. We next evaluated the urea electrosynthesis performance of these catalysts through a five-criteria screening framework (Fig. 1c): (i) Structural stability, (ii) N_2 adsorption geometry, (iii) C-N coupling feasibility, (iv) product selectivity, and (v) limiting potential (U_L), prioritized to eliminate kinetically trapped candidates. To evaluate the thermodynamic and electrochemical stability, the formation energies (E_f) and dissolution potentials (U_{diss}) of the TM-$MoSe_2$ catalysts were calculated using the following formulas:

$$E_f = E_{\text{TM-MoSe}_2} - E_{\text{Se-MoSe}_2} + n\mu_{Se} + \mu_{Mo} - \mu_{TM} \quad (5)$$

$$U_{diss} = U^0_{diss}(\text{metal,bulk}) - E_f/ne \quad (6)$$

where $E_{\text{TM-MoSe}_2}$ and $E_{\text{Se-MoSe}_2}$ are the total energy of TM-$MoSe_2$ and 100% Se-terminated $MoSe_2$, respectively. μ_{Mo} and μ_{TM} represent the total energy of the Mo and TM atoms in their most stable bulk phases, respectively. μ_{Se} was determined from $\mu_{Mo} + 2\mu_{Se} = \mu_{MoSe_2}$.[62] U^0_{diss}(metal,bulk) denotes the standard dissolution potential of the bulk metal and *n* denotes the number of electrons involved in the dissolution. Generally, catalysts with $E_f < 0$ eV and $U_{diss} > 0$ V are considered both thermodynamically and electrochemically stable. The E_f and U_{diss} values for TM-$MoSe_2$ are given in Fig.1d, and the corresponding specific values are listed in Table S4. Encouragingly, the calculated E_f values for all 22 TM-$MoSe_2$ systems are significantly below 0 eV, indicating the high thermodynamic stability. However, evaluation against the U_{diss} value reveals that the Mn-$MoSe_2$ system exhibits poor electrochemical stability, and

View Article Online
DOI: 10.1039/D5TA04475H

thus it will be excluded from subsequent calculations.

3.2 Electrosynthesis of urea on TM-$MoSe_2$

3.2.1 Adsorption of N_2. In the ER mechanism of urea synthesis, effective activation of the inert N≡N triple bond is a prerequisite for subsequent CO insertion to form the key intermediate of tower-like *NCON. To investigate this process, we systematically investigated the adsorption and activation of $^*N_2$ on TM-$MoSe_2$ catalysts. Five different adsorption configurations were considered (Fig. 2a): (1) Side-on adsorption at monometallic Mo sites; (2) End-on adsorption at monometallic Mo sites; (3) Side-on adsorption at monometallic TM sites; (4) End-on adsorption at monometallic TM sites; (5) Side-on adsorption at bimetallic Mo-TM sites. These configurations represent different interaction modes between N_2 and TM-$MoSe_2$, to explore their applicability in urea electrosynthesis. Notably, the lateral (side-on) adsorption thermodynamically favors C-N coupling by enabling efficient N≡N bond activation and optimal spatial alignment for tower-shaped *NCON precursor formation.[25] Adsorption energy calculations (Table S5) reveal TM-dependent optimal configurations (Fig. 2b). While all catalysts exhibit stable N_2 adsorption, side-on configurations consistently show more elongated N≡N bond lengths and enhanced activation. Specifically, TM-$MoSe_2$ with late transition metals (Cr, Fe, Co, Ni, Cu, Ru, Rh, Pd, Ag, Re, Os, Ir, Pt, Au) preferentially adopt end-on adsorption. In contrast, pristine $MoSe_2$ and variants doped with early transition metals (Ti, V, Zr, Nb, Hf, Ta, W) prefer side-on adsorption. Considering the pivotal role of side-on adsorbed $^*N_2$ in mediating CO insertion toward *NCON formation, subsequent mechanistic investigations specifically target pristine

View Article Online
DOI: 10.1039/D5TA04475H

and TM-incorporated $MoSe_2$ systems (TM = Ti, V, Zr, Nb, Hf, Ta, W).

To understand the influence of $^*CO$ adsorption, we calculated the co-adsorption of $^*CO$ and $^*N_2$ on $MoSe_2$ and TM-$MoSe_2$ catalysts (Table S6). The computational results indicate that stable co-adsorption states of $^*CO$ and $^*N_2$ can form on all catalysts. Notably, on Nb-$MoSe_2$, Ta-$MoSe_2$, and W-$MoSe_2$ catalysts, the adsorption energy of $^*N_2$ is stronger than that of $^*CO$ by approximately 0.02–0.27 eV. In contrast, on the other catalysts, $^*CO$ adsorption is stronger than $^*N_2$ adsorption by approximately 0.07–0.48 eV. Importantly, in the co-adsorption configuration, $^*CO$ preferentially adsorbs at the Mo-Se sites adjacent to the Mo-TM sites occupied by $^*N_2$ (Fig. S5). This spatial separation indicates that the TM-$MoSe_2$ catalysts can provide dual active sites, thereby avoiding competitive adsorption between $^*CO$ and $^*N_2$.

Furthermore, the possibility of C-N coupling between adsorbed $^*CO$ and adsorbed $^*N_2$ species was investigated. The transition state for the C-N coupling process ($^*N_2 + {}^*CO \rightarrow {}^*NCON$) was calculated on pristine $MoSe_2$ and TM-doped $MoSe_2$ (TM = Ti, V, Zr, Nb, Hf, Ta, W) catalysts. As shown in Fig. S6, the activation energy barriers on these catalysts are prohibitively high (1.06 eV to 2.12 eV), rendering the direct C-N coupling reaction energetically unfavorable. Consequently, we proceeded with the investigation of the ER mechanism.

It is noteworthy that CO, besides potentially inserting into activated $^*N_2$ to form the urea precursor $^*NCON$, may also insert into intermediates generated during subsequent steps of the NRR, such as $^*NNH$, $^*NHNH$, or $^*NHNH_2$. We compared the free energy changes (ΔG) for $^*N_2$ to $^*NCON$ formation versus its competitive intermediate $^*NNH$

View Article Online
DOI: 10.1039/D5TA04475H

formation on $MoSe_2$ and TM-$MoSe_2$ catalysts. As shown in Fig. S7, the ΔG values for $^*N_2$ to *NCON formation are significantly more negative than those for $^*N_2$ to *NNH formation on all catalysts. For example, on Nb-$MoSe_2$, the ΔG for $^*N_2$ to *NNH formation is −0.21 eV, while for *NCON formation it is −1.10 eV. This indicates a strong thermodynamic preference for forming the urea precursor *NCON over *NNH, particularly compared to subsequent NRR intermediates like *NHNH or $^*NHNH_2$. Consequently, this thermodynamic preference provides strong evidence that *NCON possesses higher stability and selectivity compared to ammonia-related species like *NNH. This demonstrates that our catalysts favor the reaction pathway via the ER mechanism, where CO inserts into activated $^*N_2$ to form the urea precursor *NCON.

3.2.2 Electrosynthesis reactions of urea. In urea synthesis, the elevated free energy change (ΔG) necessitates overcoming substantial activation barriers, reflecting poor catalytic efficiency. Previous research identified three possible thermodynamically unfavorable steps in the reaction pathway: (1) C-N coupling between $^*N_2$ and CO ($^*N_2$ + CO → *NCON); (2) Third protonation-hydrogenation step (*NHCONH + H^+ + e^-→ $^*NHCONH_2$); (3) Final protonation urea generation ($^*NHCONH_2$ + H^+ + e^- → $^*NH_2CONH_2$).[19] Notably, the C-N coupling step (*CO + $^*N_2$ → *NCON) represents a thermochemical process independent of electron transfer, where exothermic characteristics favor urea precursor formation.[13] To ensure favorable reaction kinetics, we established dual thermodynamic criteria: ΔG < 0 eV for the C-N coupling step (ensuring spontaneity) and ΔG < 0.50 eV for protonation-hydrogenation steps (balancing energy efficiency and reaction rate).[23,26] The calculated ΔG values for three

View Article Online
DOI: 10.1039/D5TA04475H

steps on $MoSe_2$ and TM-$MoSe_2$ (TM = Ti, V, Zr, Nb, Hf, Ta, W) are shown in Fig. 2c. All investigated catalysts exhibit negative ΔG values for the C-N coupling reaction, confirming the thermodynamic favorability of this process. This spontaneous behavior strongly supports urea precursor formation on all catalysts. However, pristine $MoSe_2$ and V-, Ta-, and W-doped systems were excluded from consideration because their protonation-hydrogenation steps (Steps 2–3) exceed the ΔG threshold of 0.50 eV. Therefore, Ti-, Zr-, Nb-, and Hf-doped $MoSe_2$ emerge as potential catalyst candidates that meet all screening criteria. These systems will undergo a detailed investigation to elucidate the urea synthesis mechanism. In addition, pristine $MoSe_2$ will be retained as a baseline reference to quantify the catalytic enhancement induced by transition metal doping.

3.3 Reaction mechanism on screened TM-$MoSe_2$

The detailed pathways of urea synthesis on pristine and Ti-, Zr-, Nb-, and Hf-doped $MoSe_2$ were investigated to identify the potential-determining steps. Fig. 3a shows the schematic structure of intermediates in urea electrosynthesis, while Fig. 3b-f present Gibbs free energy diagrams for pristine and Ti-, Zr-, Nb-, and Hf-doped $MoSe_2$ catalysts, with adsorption configurations detailed in Fig. S8. As shown in Fig. 3b–f, the electrosynthesis of urea over these five catalysts follows the same reaction path, i.e. $* \rightarrow {}^*N_2 \rightarrow {}^*NCON \rightarrow {}^*NCONH \rightarrow {}^*NHCONH \rightarrow {}^*NHCONH_2 \rightarrow {}^*NH_2CONH_2$. The former two steps to form *NCON ($* \rightarrow {}^*N_2 \rightarrow {}^*NCON$) are all downhill processes. For the C-N coupling step (${}^*N_2 \rightarrow {}^*NCON$), the ΔG values on $MoSe_2$, Ti-$MoSe_2$, Zr-$MoSe_2$, Nb-$MoSe_2$, and Hf-$MoSe_2$ catalysts were −1.43, −0.73, −0.80, −1.10, and −0.76 eV,

View Article Online
DOI: 10.1039/D5TA04475H

respectively, indicating that these catalysts can thermodynamically promote the C-N coupling spontaneously. Structural analyses of the *NCON intermediate reveal N≡N bond cleavage (about 2.30 Å) with simultaneous formation of dual C-N bonds (1.40 Å), confirming its successful generation through C-N coupling. Following the formation of the *NCON intermediate, catalytic hydrogenation proceeds through two distinct pathways: exothermic reduction to *NCONH ($\Delta G < 0$ eV), followed by bifurcation into either the high-energy distal product $^*NCONH_2$ ($\Delta G = 0.09$ to 0.52 eV) or the thermodynamically favored alternate product *NHCONH ($\Delta G = -0.58$ to -0.33 eV). The *NHCONH intermediate subsequently undergoes endergonic hydrogenation to $^*NHCONH_2$ ($\Delta G > 0$ eV), culminating in the final urea formation step ($^*NHCONH_2 \rightarrow {}^*NH_2CONH_2$). Rate-determining step (RDSs) are identified as follows: $MoSe_2$ and Ti-$MoSe_2$ exhibit the highest barriers at the final step, measuring 0.79 and 0.28 eV, respectively. In contrast, Zr-, Nb-, and Hf-doped catalysts show maximum energy barriers during the penultimate transition from *NHCONH to $^*NHCONH_2$, with values of 0.26, 0.35, and 0.35 eV, respectively. Based on the ΔG of RDSs, the limiting potential (U_L) was further calculated. As shown in Fig. 3, the U_L of TM-doped catalysts exhibits marked improvements in urea electrosynthesis activity compared to the undoped $MoSe_2$ substrate (−0.79 V). Zr-$MoSe_2$ demonstrates the most favorable thermodynamics with a U_L of -0.26 V, followed by Ti-$MoSe_2$ (−0.28 V), Nb-$MoSe_2$ (−0.35 V), and Hf-$MoSe_2$ (−0.35 V). These values not only surpass the performance of conventional PdCu catalysts (−0.64 V)[9] but also outperform ReV@C_2N (−0.69 V),[13] MBenes materials (−0.49 to −0.65 V),[23] and Ti@g-C_3N_4 (−0.42 V),[63] highlighting the

View Article Online
DOI: 10.1039/D5TA04475H

superior catalytic efficiency achieved through strategic transition metal doping.

Finally, the generated urea $^{*}NH_2CONH_2$ will be desorbed from the TM-$MoSe_2$ catalysts. It is essential to ensure that urea molecules desorb weakly to quickly restore the catalytically active sites, facilitating a smooth progression into the next catalytic cycle. The desorption energy of urea molecules on Ti-, Zr-, and Nb-doped $MoSe_2$ are calculated to be −1.02 eV, −1.17 eV, and −1.18 eV, significantly lower than that on $PdCu/TiO_2$ (−1.68 eV),[9] 2D Mo_2B_2 (−1.28 eV), Ti_2B_2 (−1.55 eV), and Cr_2B_2 (−1.21 eV).[23] The desorption energy on Hf-$MoSe_2$ (−1.29 eV) marginally exceeds that on Mo_2B_2 (−1.28 eV) and Cr_2B_2 (−1.21 eV).[23] This suggests that TM-$MoSe_2$ exhibits superior urea release capability during electrochemical reactions in flow cell systems.

Since urea electrosynthesis occurs in aqueous solutions, we evaluated solvent effects on the catalytic activity of the model Nb-doped $MoSe_2$ system. Using an implicit solvation model, we recalculated Gibbs free energy profiles for urea synthesis on Nb-$MoSe_2$ and present the corresponding energy diagram in Fig. S9. Calculations suggest that the potential-determining step remains unchanged when incorporating solvent effects compared to gas-phase simulations, with only a 0.05 V variation in U_L. This demonstrates that Nb-$MoSe_2$ maintains its superior urea electrosynthesis performance regardless of solvent interactions.

It is worth noting that the key C-N coupling step in urea electrosynthesis is a non-electrochemical reaction. Therefore, the kinetic barrier of the C-N coupling needs to be considered. Herein, we calculated the energy barrier for the $^{*}N_2$ reaction with $^{*}CO$ to form C-N bonds (Fig. S10). The results show that the kinetic energy barrier of C-N

View Article Online
DOI: 10.1039/D5TA04475H

coupling on Nb-$MoSe_2$ is 0.64 eV, which is much lower than those on PdCu (0.79 eV),[24] Fe/p-BN (1.14 eV),[25] and Co/p-BN (0.75 eV) catalysts,[25] which demonstrates the kinetic feasibility of the coupling of $^*N_2$ and $^*CO$ on the Nb-$MoSe_2$ catalyst.

3.4 Selectivity of urea synthesis

Competing side reactions (NRR and HER) can significantly reduce the Faradaic efficiency of urea synthesis.[26] To ensure high selectivity for urea production, the limiting potential for urea synthesis (U_L^{Urea}) should be lower than those of NRR (U_L^{NRR}) and HER (U_L^{HER}), i.e., $U_L^{Urea} > U_L^{NRR}$ and U_L^{HER}. Therefore, the Gibbs free energy diagrams of NRR and HER were calculated for Ti-$MoSe_2$, Zr-$MoSe_2$, Nb-$MoSe_2$, Hf-$MoSe_2$, as well as pristine $MoSe_2$ (Fig. 4 and Figs. S11–S13). As shown in Fig. 4a and Fig. S11, the U_L^{NRR} is as high as −0.5 eV to −0.8 eV for all four catalysts as well as the pristine substrate in the NRR process. For Nb-$MoSe_2$, the limiting potential (U_L^{NRR}) of NRR reaches −0.80 V, which is significantly more negative than the U_L^{Urea} of −0.35 V observed during urea electrosynthesis. This notable difference in electrochemical driving forces indicates that the C-N coupling process preferentially proceeds to generate urea products, effectively suppressing the competing pathway for NH_3 byproduct formation.

The HER on $MoSe_2$ and TM-$MoSe_2$ (TM = Ti, Zr, Nb, Hf) was further calculated (Fig. 4b and Fig. S13). As shown in Fig. S13, protons are more readily adsorbed at the center between Mo and TM at the edge of TM-$MoSe_2$. Therefore, these metal atoms can directly receive proton-electron pairs, resulting in the production of $^*H$. If this reaction continues, hydrogen (H_2) byproducts will be formed and desorbed from the

View Article Online
DOI: 10.1039/D5TA04475H

catalyst surface, leading to a drastic reduction of the selectivity of urea. As shown in Fig. 4b, the hydrogen evolution on all five catalysts is poor. Among them, Nb-doped $MoSe_2$ is the most effective in inhibiting the competitive HER, and the corresponding U_L^{HER} reaches −0.72 V, significantly lower than that of U_L^{Urea} (−0.35 V).

To further determine the urea selectivity of TM-$MoSe_2$ catalysts, we calculated the difference between U_L^{Urea} with U_L^{NRR} and U_L^{HER} (Fig. 4c). The values of U_L^{Urea} - U_L^{NRR} and U_L^{Urea} - U_L^{HER} on pristine $MoSe_2$ are −0.11 V and −0.13 V, respectively, indicating that thermodynamically favor competing NRR and HER pathways, hindering the production of urea. This selectivity limitation persists in Hf-$MoSe_2$ (U_L^{Urea} - U_L^{HER} = −0.01 V), albeit with reduced severity. Remarkably, Ti-, Zr-, and Nb-doped catalysts exhibit positive potential difference, establishing an electrochemical window where urea synthesis becomes thermodynamically dominant. Particularly noteworthy is Nb-$MoSe_2$, positioned in the optimal quadrant of Fig. 4c with the largest potential difference (U_L^{Urea} - U_L^{NRR} = +0.53 V; U_L^{Urea} - U_L^{HER} = +0.35 V). The significant positive potential differences suggest that Nb-$MoSe_2$ can completely suppress the NRR/HER pathways, enhancing Faradaic efficiency in urea electrosynthesis.

3.5 Source of activity of Nb-$MoSe_2$

In the catalytic reaction, the adsorption and activation of reactants play a decisive role. To further explore the excellent performance of Nb-$MoSe_2$, the charge density difference and partial density of states (PDOS) of its adsorbed $^*N_2$ were analyzed in detail. The charge density difference plot (Fig. 5a) shows that the two N atoms of $^*N_2$ form effective chemical bonds with Mo and Nb, respectively. $^*N_2$ acquires electrons

View Article Online
DOI: 10.1039/D5TA04475H

from the Mo-Nb bimetal, with the electrons residing on the N-Mo and N-Nb bonds (green colour). This induces charge dissipation in the N≡N bond (yellow colour), suggesting that the synergistic effect of Mo and Nb effectively weakens the N≡N bond and facilitates subsequent CO insertion. The PDOS diagram (Fig. 5b) indicates strong p-d orbital matching between the p orbitals of $^{*}N_2$ and the d orbitals of both Mo and Nb atoms near the Fermi level. This reveals orbital hybridization and electron transfer between $^{*}N_2$ and the bimetal system, further confirming the successful activation of the N≡N bond. In addition, the Fermi energy level is in a continuous and non-zero density of electronic states, indicating that the catalyst structure of Nb-$MoSe_2$ has good electrical conductivity.

Our calculations identified two thermodynamically unfavorable steps in the urea synthesis process on TM-$MoSe_2$, corresponding to the final two hydrogenation stages, where the progressively increasing ΔG hinders the kinetics of urea formation. To probe these barriers, we systematically quantified the ΔG values of these steps alongside the adsorption energies (ΔE) of the intermediates $^{*}NHCONH$ and $^{*}NH_2CONH_2$. As shown in Fig. S14, the ΔG values exhibit strong linear correlations with $\Delta E_{*NHCONH}$ (R^2 = 0.89) and $\Delta E_{*NH_2CONH_2}$ (R^2 = 0.83), respectively. Importantly, tuning $\Delta E_{*NHCONH}$ and $\Delta E_{*NH_2CONH_2}$ within the thresholds of −6.98 to −6.48 eV and −1.29 to −1.02 eV, respectively, can keep ΔG in an ultralow range, favoring urea formation. Therefore, these ΔE intervals can serve as robust descriptors for high-throughput screening of efficient urea synthesis catalysts.

However, screening by two reaction intermediates, $^{*}NHCONH$ and $^{*}NH_2CONH_2$,

View Article Online
DOI: 10.1039/D5TA04475H

still has a large workload, so we worked on finding other descriptors to screen the catalysts more efficiently. Fig. 5c shows the volcano curves between the limit potential U_L of urea synthesis and the adsorption free energy of intermediate *NCON (ΔG_{*NCON}) on TM-$MoSe_2$ catalysts. It can be observed that the catalytic activity of urea synthesis is poor when the binding strength of *NCON is too strong (e.g., $MoSe_2$, Ta-$MoSe_2$, and W-$MoSe_2$) or too weak (e.g., V-$MoSe_2$). In contrast, Ti-$MoSe_2$, Zr-$MoSe_2$, Nb-$MoSe_2$, and Hf-$MoSe_2$ are located at the top of the volcano curves, suggesting that the adsorption of *NCON on these catalysts reaches the optimal binding strength for promoting urea synthesis. Therefore, ΔG_{*NCON} can be used as an effective indicator to characterize the activity of catalysts for urea synthesis, with optimal adsorption free energies ranging from −2.28 to −1.59 eV. In addition, we found an approximately linear correlation between the N≡N bond lengths of $^*N_2$ and the ΔG values of *NCON (R^2 = 0.87, see Fig. 5d). This correlation suggests that ΔG_{*NCON} gradually decreases as the N≡N bond length increases. Therefore, a suitable N≡N bond length (−1.19 to −1.22 Å) can balance the magnitude of ΔG_{*NCON} and thus facilitate urea electrosynthesis.

Finally, we performed AIMD simulations of the Nb-$MoSe_2$ catalyst to evaluate its thermal stability. As shown in Fig. 6, after 10 ps of simulations at temperatures of 300 K and 500 K, the Nb-$MoSe_2$ catalyst maintains a stable energy profile and retains structural integrity, with no observable bond rupture or structural reconstruction. These findings conclusively demonstrate the exceptional thermal stability of Nb-$MoSe_2$ under elevated temperature conditions. Overall, the screened Nb-$MoSe_2$ catalysts exhibit good thermodynamic, electrochemical, and thermal stability, which ensures their

View Article Online
DOI: 10.1039/D5TA04475H

practical application in the electrocatalytic synthesis of urea.

3.6 Outlook on alternative C–N coupling mechanisms

Recent studies[64] indicate an alternative pathway for urea synthesis where CO undergoes stepwise coupling with ammonia species generated during the NRR. In this mechanism, adsorbed N_2 is first protonated to form $^*NH_xNH_y$ intermediates. These $^*NH_xNH_y$ species subsequently dissociate. CO then undergoes an initial C-N coupling with a dissociated $^*NH_x$ fragment to form $^*NH_xCO$, followed by a second C-N coupling with another dissociated NH_y species to yield $^*NH_xCONH_y$. Protonation steps ultimately produce urea. To evaluate this pathway on our screened catalysts, we calculated the transition states for stepwise coupling on Nb-$MoSe_2$. The results confirm that CO can undergo stepwise C-N coupling with NRR-derived ammonia species at low energy barriers (0.12 eV to 0.83 eV, Figs. S16-S18). For example, the pathway involving CO + $^*NHNH \rightarrow$ CO + $^*NH$ + $^*NH \rightarrow$ $^*NHCO$ + $^*NH \rightarrow$ $^*NHCONH$ exhibits energy barriers of only 0.32 eV, 0.54 eV, and 0.16 eV for the key dissociation and coupling steps, respectively. Consequently, catalysts that thermodynamically and kinetically favor the initial NRR steps to form $^*NH_xNH_y$ intermediates hold significant promise for efficient urea electrosynthesis through this stepwise C-N coupling mechanism.

4. Conclusion

In this work, the edge-active sites of 2H-$MoSe_2$ nanoribbons doped with 3d–5d TM atoms were systematically screened via DFT calculations to evaluate their potential for electrocatalytic coupling of N_2 and CO toward urea synthesis. Theoretical results

View Article Online
DOI: 10.1039/D5TA04475H

demonstrate that Nb-$MoSe_2$ exhibits exceptional catalytic performance for urea electrosynthesis, attributed to its superior structural stability, ultralow limiting potential (−0.35 V), reduced kinetic barrier (0.64 eV), and effective suppression of competing side reactions (e.g., NRR and HER). Furthermore, computational data reveal a strong correlation between the catalytic activity (quantified by the limiting potential, U_L) of TM-$MoSe_2$ catalysts and their binding strength to the *NCON intermediate (ΔG_{*NCON}), which linearly correlates with bond-length variations in adsorbed $^*N_2$ molecules. The enhanced activity of Nb-$MoSe_2$ originates from the synergistic electronic effect between Nb and Mo atoms, which facilitates efficient $^*N_2$ activation through orbital hybridization. This study not only highlights the promise of Nb-doped $MoSe_2$ edge sites for urea electrosynthesis but also expands the applicability of TMDs in advanced electrocatalytic systems.

Conflict of interest

The authors declare that there is no financial or personal relationships that may be perceived as influencing their work.

Author Contributions

Jing Xu and Lianming Zhao conceived and supervised the study and drafted the manuscript. Ye Shi performed the theoretical calculations. Yizhu Wang, Shouao Li, Yuan Li, Xueru Wang, and Jinghao Zhang were responsible for data curation. Hao Ren, Wei Xing and Guang Zhao participated in data discussion. All authors reviewed and commented on the manuscript.

Data availability

View Article Online
DOI: 10.1039/D5TA04475H

The data that supports the findings of this study are available on request from the corresponding author Dr Lianming Zhao upon reasonable request.

Acknowledgments

This work was supported by the National Natural Science Foundation of China (U23B2087) and Shandong Provincial Natural Science Foundation (ZR2022MB094).

References

1 J. W. Erisman, M. A. Sutton, J. Galloway, Z. Klimont and W. Winiwarter, *Nat. Geosci*, 2008, **1**, 636–639.

2 B. M. Comer, P. Fuentes, C. O. Dimkpa, Y.-H. Liu, C. A. Fernandez, P. Arora, M. Realff, U. Singh, M. C. Hatzell and A. J. Medford, *Joule*, 2019, **3**, 1578–1605.

3 L. Celleno, *Dermatol. Ther*, 2018, **31**, e12690.

4 A. A. Younis, *J. Ind. Text*, 2020, **49**, 791–808.

5 G. Gnana kumar, A. Farithkhan and A. Manthiram, *Adv. Energy. Sustain. Res*, 2020, **1**, 2000015.

6 C. Lv, L. Zhong, H. Liu, Z. Fang, C. Yan, M. Chen, Y. Kong, C. Lee, D. Liu, S. Li, J. Liu, L. Song, G. Chen, Q. Yan and G. Yu, *Nat. Sustain*, 2021, **4**, 868–876.

7 D. R. MacFarlane, P. V. Cherepanov, J. Choi, B. H. R. Suryanto, R. Y. Hodgetts, J. M. Bakker, F. M. Ferrero Vallana and A. N. Simonov, *Joule*, 2020, **4**, 1186–1205.

8 Z. Mei, Y. Zhou, W. Lv, S. Tong, X. Yang, L. Chen and N. Zhang, *ACS. Sustain. Chem. Eng*, 2022, **10**, 12477–12496.

9 C. Chen, X. Zhu, X. Wen, Y. Zhou, L. Zhou, H. Li, L. Tao, Q. Li, S. Du, T. Liu, D.

View Article Online
DOI: 10.1039/D5TA04475H

Yan, C. Xie, Y. Zou, Y. Wang, R. Chen, J. Huo, Y. Li, J. Cheng, H. Su, X. Zhao, W. Cheng, Q. Liu, H. Lin, J. Luo, J. Chen, M. Dong, K. Cheng, C. Li and S. Wang, *Nat. Chem.*, 2020, **12**, 717–724.

10 L. Ma, J. Yuan, Z. Liu, Y. Luo, Y. Su, K. Zhu, Z. Feng, H. Niu, S. Xiao, J. Wei and X. Xiang, *ACS Appl. Mater. Interfaces*, 2024, **16**, 26015–26024.

11 Z.-H. Zhao, R. Jiang, H. Niu, M. Wang, J. Wang, Y. Du, Y. Tian, M. Yuan, G. Zhang and Z. Lu, *J. Colloid. Interface. Sci*, 2025, **682**, 222–231.

12 W. Zhang, M. Qu, A. Du and Q. Sun, *J. Mater. Sci*, 2024, **59**, 5426–5435.

13 C. Liu, F. Gong, Q. Zhou and Y. Xie, *Energy. Fuels*, 2024, **38**, 8951–8959.

14 D. Jiao, Z. Wang, Y. Liu, Q. Cai, J. Zhao, C. R. Cabrera and Z. Chen, *Energy Environ. Mater.*, 2024, **7**, e12496.

15 D. Jiao, Y. Dong, X. Cui, Q. Cai, C. R. Cabrera, J. Zhao and Z. Chen, *J. Mater. Chem. A*, 2022, **11**, 232–240.

16 M. Yuan, H. Zhang, Y. Xu, R. Liu, R. Wang, T. Zhao, J. Zhang, Z. Liu, H. He, C. Yang, S. Zhang and G. Zhang, *Chem. Catal*, 2022, **2**, 309–320.

17 M. Yuan, J. Chen, Y. Xu, R. Liu, T. Zhao, J. Zhang, Z. Ren, Z. Liu, C. Streb, H. He, C. Yang, S. Zhang and G. Zhang, *Energy. Environ. Sci*, 2021, **14**, 6605–6615.

18 Y. Cao, Y. Meng, R. An, X. Zou, H. Huang, W. Zhong, Z. Shen, Q. Xia, X. Li and Y. Wang, *J. Colloid. Interface. Sci*, 2023, **641**, 990–999.

19 C. Zhu, M. Wang, C. Wen, M. Zhang, Y. Geng, G. Zhu and Z. Su, *Adv. Sci*, 2022, **9**, 2105697.

20 D. J. Díaz, A. K. Darko and L. McElwee-White, *Eur. J. Org. Chem*, 2007, **2007**,

View Article Online
DOI: 10.1039/D5TA04475H

4453–4465.

21 D. M. Pinto-Zevallos, O. Skaldina and J. D. Blande, *Glob. Change. Biol*, 2025, **31**, e70034.

22 J. Du, H. Wang, C. Yue, I. Ali Soomro, M. Pu and M. Lei, *Appl. Surf. Sci*, 2024, **658**, 159854.

23 X. Zhu, X. Zhou, Y. Jing and Y. Li, *Nat. Commun*, 2021, **12**, 4080.

24 J. Peng, X. Wang, Z. Wang, B. Liu, P. Zhang, X. Li and N. Li, *Chin. J. Struct. Chem*, 2022, **41**, 2209094–2209104.

25 L. Kong, D. Jiao, Z. Wang, Y. Liu, Y. Shang, L. Yin, Q. Cai and J. Zhao, *Chem. Eng. J*, 2023, **451**, 138885.

26 J. Zhong, D. Gao, Z. Liu, Y. Yu, C. Yu, Y. Fang, J. Lin, C. Tang and Z. Guo, *Fuel*, 2024, **366**, 131280.

27 E. Son, S. Lee, J. Seo, U. Kim, S. H. Kim, J. M. Baik, Y.-K. Han and H. Park, *ACS Nano*, 2023, **17**, 10817–10826.

28 D. M. Khaidar, W. N. R. W. Isahak, Z. A. C. Ramli and K. N. Ahmad, *Int. J. Hydrogen. Energy*, 2024, **68**, 35–50.

29 L. Wang, Z. Wen and G. Luo, *J. Phys. Chem. Lett.*, 2025, **16**, 969–974.

30 D. Kong, H. Wang, J. J. Cha, M. Pasta, K. J. Koski, J. Yao and Y. Cui, *Nano Lett.*, 2013, **13**, 1341–1347.

31 C.-P. Yang, S. Xin, Y.-X. Yin, H. Ye, J. Zhang and Y.-G. Guo, *Angew. Chem. Int. Ed*, 2013, **52**, 8363–8367.

32 X. Wu, Y. Wang, P. Li and Z. Xiong, *Superlattices. Microstruct*, 2020, **139**, 106388.

View Article Online
DOI: 10.1039/D5TA04475H

33 J. Guo, H. Dong, J. Liu, J. Guan, K. Li, Y. Feng, Q. Liu, J. Yang and H. Geng, *J. Colloid. Interface. Sci*, 2023, **652**, 1427–1437.

34 C. Yang, L. Zhou, C. Wang, W. Duan, L. Zhang, F. Zhang, J. Zhang, Y. Zhen, L. Gao, F. Fu and Y. Liang, *Appl. Catal. B. Environ*, 2022, **304**, 120993.

35 S. Deng, Y. Zhong, Y. Zeng, Y. Wang, Z. Yao, F. Yang, S. Lin, X. Wang, X. Lu, X. Xia and J. Tu, *Adv. Mater*, 2017, **29**, 1700748.

36 S.-H. Lin and J.-L. Kuo, *Phys. Chem. Chem. Phys*, 2015, **17**, 29305–29310.

37 A. Jain, M. B. Sadan and A. Ramasubramaniam, *J. Phys. Chem. C*, 2020, **124**, 12324–12336.

38 O. Lehtinen, H.-P. Komsa, A. Pulkin, M. B. Whitwick, M.-W. Chen, T. Lehnert, M. J. Mohn, O. V. Yazyev, A. Kis, U. Kaiser and A. V. Krasheninnikov, *ACS Nano*, 2015, **9**, 3274–3283.

39 D. Gao, B. Xia, C. Zhu, Y. Du, P. Xi, D. Xue, J. Ding and J. Wang, *J. Mater. Chem. A*, 2018, **6**, 510–515.

40 V. Kuraganti, A. Jain, R. Bar-Ziv, A. Ramasubramaniam and M. Bar-Sadan, *ACS Appl. Mater. Interfaces*, 2019, **11**, 25155–25162.

41 J. Jiang, G. Wu, M. Sun, Y. Liu, Y. Yang, A. Du, L. Dai, X. Mao and Q. Qin, *ACS Nano*, 2024, **18**, 13745–13754.

42 J. P. Perdew, K. Burke and M. Ernzerhof, *Phys. Rev. Lett.*, 1996, **77**, 3865–3868.

43 M. Ernzerhof and G. E. Scuseria, *J. Chem. Phys*, 1999, **110**, 5029–5036.

44 H.-P. Komsa and A. V. Krasheninnikov, *Phys. Rev. B*, 2012, **86**, 241201.

45 S. Barja, S. Wickenburg, Z.-F. Liu, Y. Zhang, H. Ryu, M. M. Ugeda, Z. Hussain,

View Article Online
DOI: 10.1039/D5TA04475H

Z.-X. Shen, S.-K. Mo, E. Wong, M. B. Salmeron, F. Wang, M. F. Crommie, D. F. Ogletree, J. B. Neaton and A. Weber-Bargioni, *Nat. Phys*, 2016, **12**, 751–756.

46 Y. Ouyang, C. Ling, Q. Chen, Z. Wang, L. Shi and J. Wang, *Chem. Mater.*, 2016, **28**, 4390–4396.

47 H. Shu, D. Zhou, F. Li, D. Cao and X. Chen, *ACS Appl. Mater. Interfaces*, 2017, **9**, 42688–42698.

48 M. Cococcioni and S. de Gironcoli, *Phys. Rev. B*, 2005, **71**, 035105.

49 S. Grimme, J. Antony, S. Ehrlich and H. Krieg, *J. Chem. Phys.*, 2010, **132**, 154104 .

50 J. Wu and Y.-X. Yu, *J. Colloid Interface Sci.*, 2022, **623**, 432–444.

51 W. Zhao, L. Chen, W. Zhang and J. Yang, *J. Mater. Chem. A*, 2021, **9**, 6547–6554.

52 S. Zhu, M. Qin, L. Chen, S. Jiang, Y. Zhou, J. Jiang and W. Zhang, *J. Phys. Chem. Lett.*, 2023, **14**, 4185–4191.

53 B. Delley, *Phys. Rev. B*, 2002, **66**, 155125.

54 A. Zagdoun, A. J. Rossini, D. Gajan, A. Bourdolle, O. Ouari, M. Rosay, W. E. Maas, P. Tordo, M. Lelli, L. Emsley, A. Lesage and C. Copéret, *Chem. Commun.*, 2011, **48**, 654–656.

55 T. A. Halgren and W. N. Lipscomb, *Chem. Phys. Lett*, 1977, **49**, 225–232.

56 G. Martyna, M. Klein and M. Tuckerman, *J. Chem. Phys*, 1992, **97**, 2635–2643.

57 Y. Ding, L. Zhao, Y. Tong, W. Kong, B. Li, J. Wang, X. Han, W. Xing and J. Xu, *J. Phys. Chem. C*, 2022, **126**, 13617–13628.

58 A. A. Peterson, F. Abild-Pedersen, F. Studt, J. Rossmeisl and J. K. Nørskov, *Energy Environ. Sci.*, 2010, **3**, 1311–1315.

View Article Online
DOI: 10.1039/D5TA04475H

59 J. K. Nørskov, J. Rossmeisl, A. Logadottir, L. Lindqvist, J. R. Kitchin, T. Bligaard and H. Jónsson, *J. Phys. Chem. B*, 2004, **108**, 17886–17892.

60 L. Yang, H. Wang, X. Wang, W. Luo, C. Wu, C. Wang and C. Xu, *Inorg. Chem.*, 2020, **59**, 12941–12946.

61 Y. Chen, S. Zhao, Y. Zhang, Y. Li, X. Gu, K. Chen, J. Xue and Q. Huang, *AI. Mater*, 2025, **1**, 1–2.

62 Y. Zhao, J. Tu, Y. Sun, X. Hu, J. Ning, W. Wang, F. Wang, Y. Xu and L. He, *J. Phys. Chem. C*, 2018, **122**, 26570–26575.

63 L. Cheng, Z. Cheng, M. Fan, Y. Ren, Y. Liu, T. Yuan and Z. Shen, *Electrochim. Acta*, 2023, **470**, 143283.

64 R. Li, J. Zhang, C. Wang and W. Guo, *J. Mater. Chem. A*, 2025, **13**, 3023–3033.

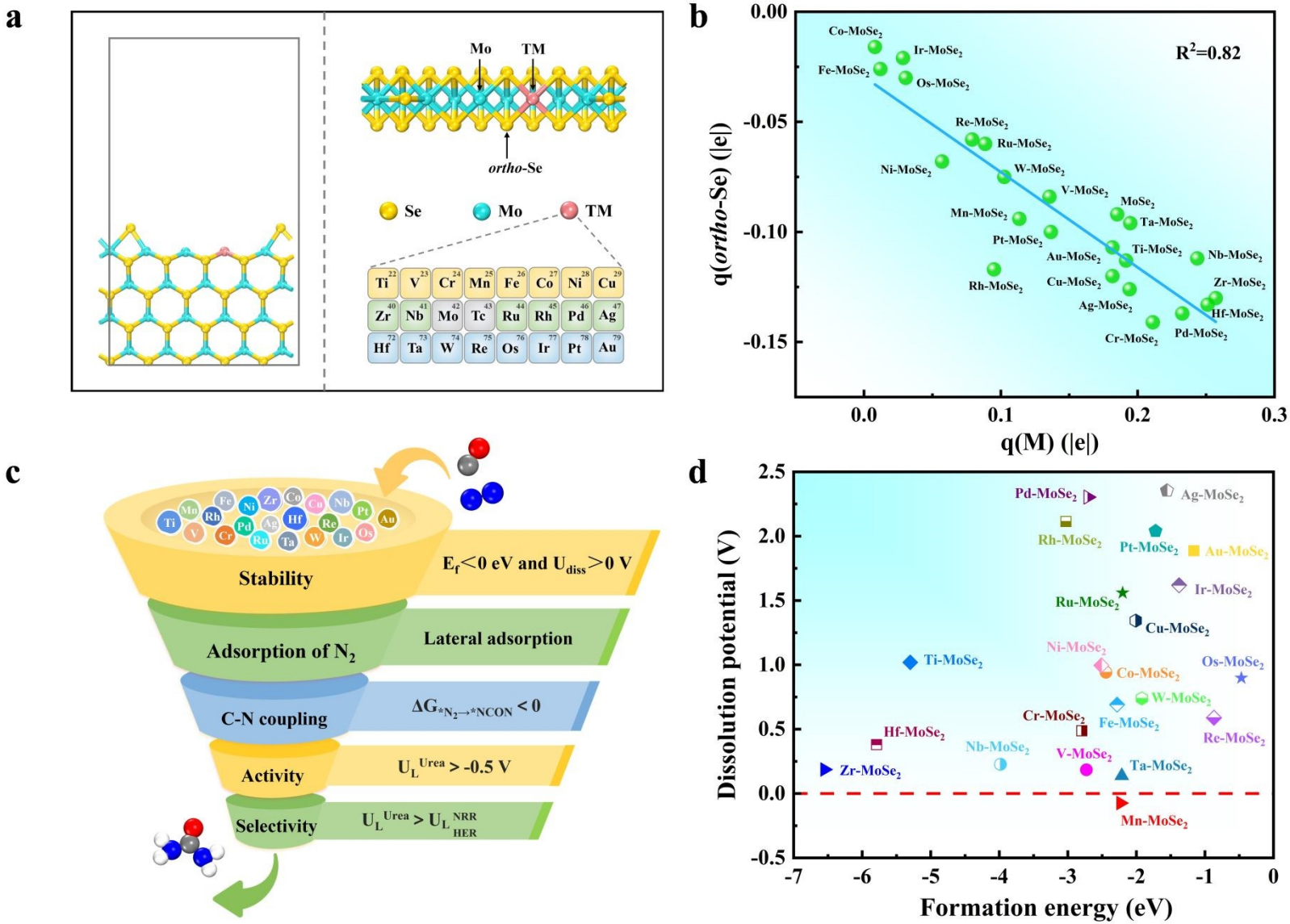

Fig.1 (a) Geometric structure of TM-$MoSe_2$ and the considered 22 transition metals. (b) The relationship of Hirshfeld charges between the bimetallic M and *ortho*-Se. (c) Depiction of screening chart flow. The blue, gray, red and white balls represent N, C, O, and H atoms, respectively. (d) Calculated formation energy and dissolution potential.

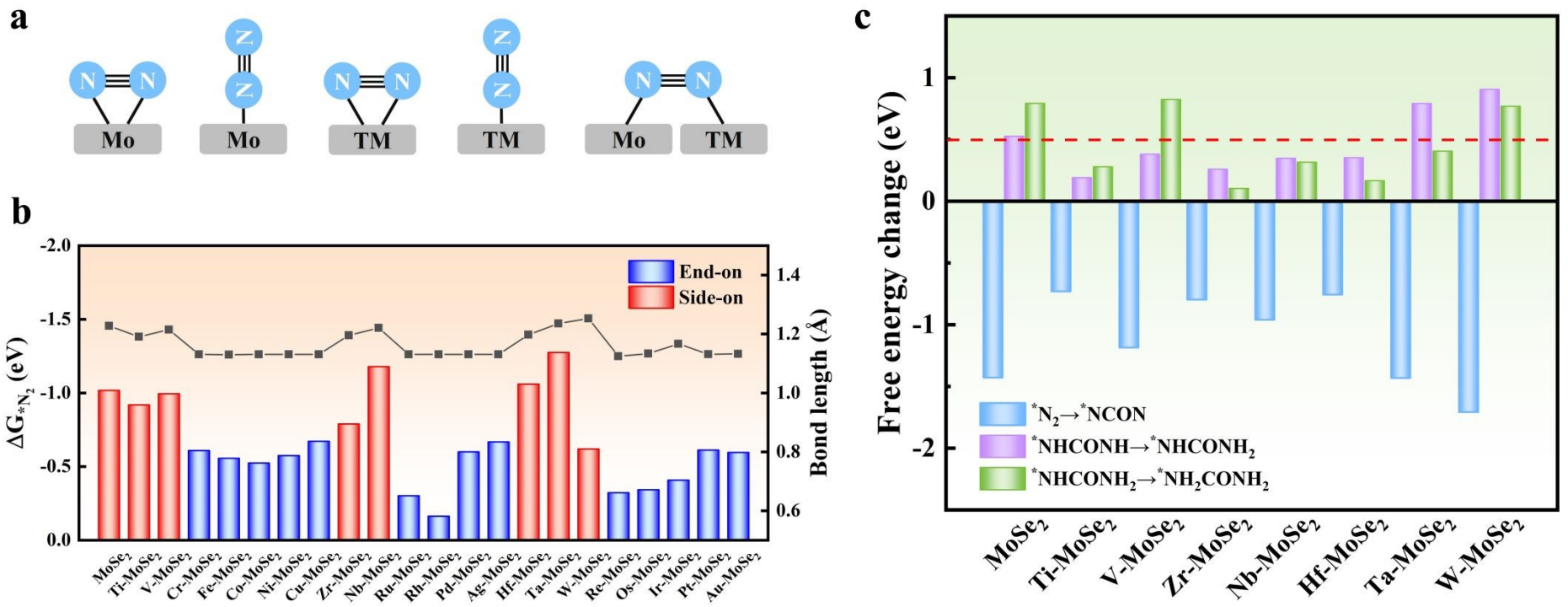

Fig.2 (a) Schematic illustration of adsorption configurations of $^*N_2$ on TM-$MoSe_2$. (b) Calculated free energies and corresponding N≡N bond lengths for the most stable adsorption configuration of $^*N_2$. (c) Calculated free energy changes for three key steps ($^*N_2$ + CO → *NCON, *NHCONH + H^+ + e^- → $^*NHCONH_2$, $^*NHCONH_2$ + H^+ + e^- → $^*NH_2CONH_2$) on eight systems. The ΔG value of 0.50 eV for three key steps is set as a criterion, marked in a red dotted line.

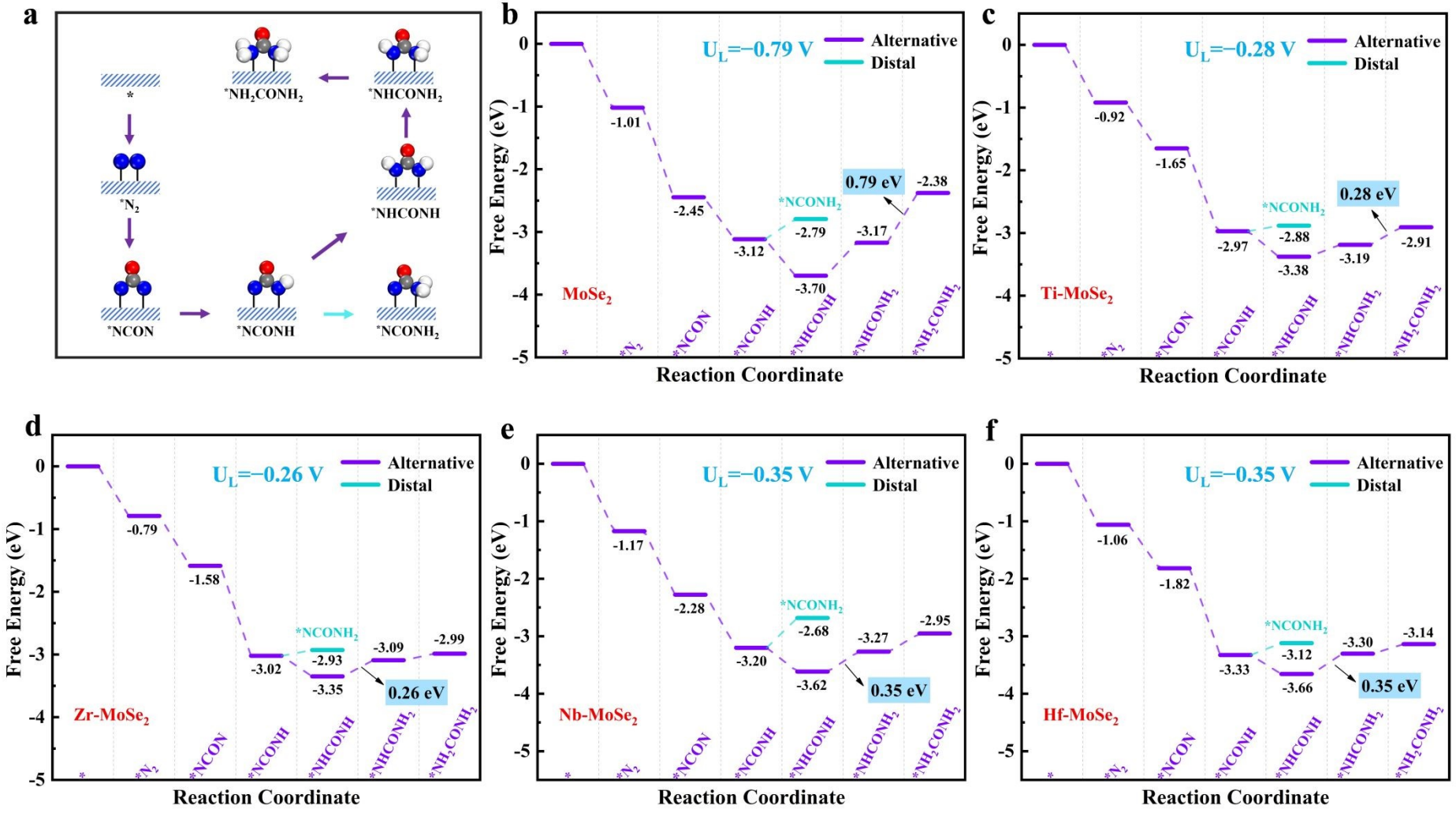

Fig.3 (a) Schematic structure of reaction intermediates in the urea electrosynthesis process. The blue, gray, red and white balls represent N, C, O, and H atoms, respectively. The two vertical lines indicate the coordination bonds between the reaction intermediates and the metal center of catalysts. Free energy diagrams for urea electrosynthesis on (b) $MoSe_2$, (c) Ti-$MoSe_2$, (d) Zr-$MoSe_2$, (e) Nb-$MoSe_2$ and (f) Hf-$MoSe_2$.

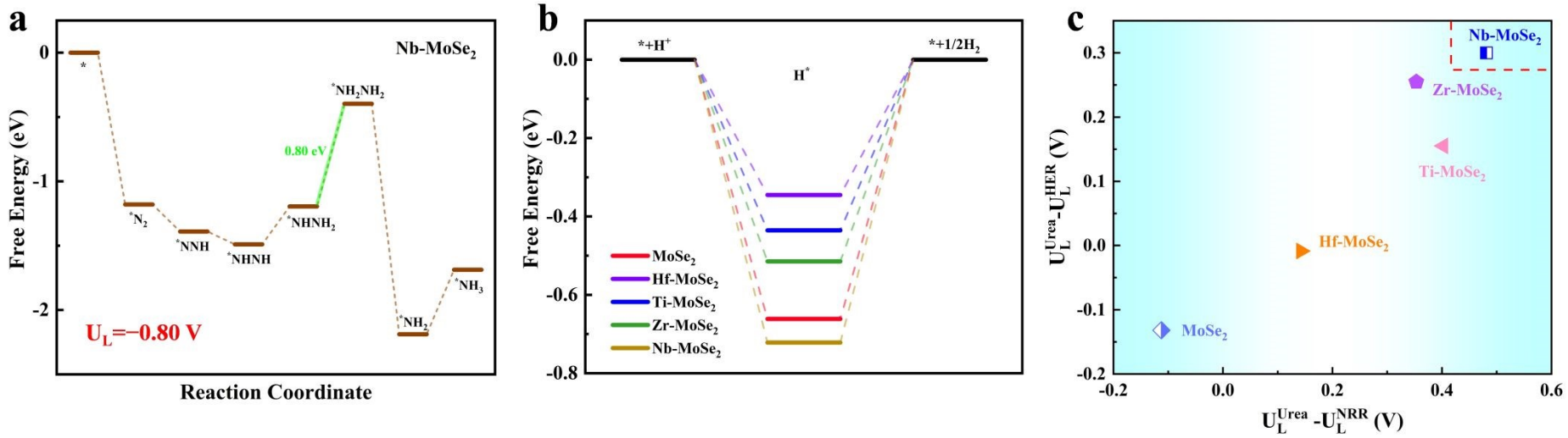

Fig.4 (a) Free energy diagram for NRR on Nb-$MoSe_2$. (b) Free energy diagrams for HER on five systems. (c) Computed limiting potential difference between urea synthesis and NRR ($U_L^{Urea} - U_L^{NRR}$) versus that between urea synthesis and HER ($U_L^{Urea} - U_L^{HER}$).

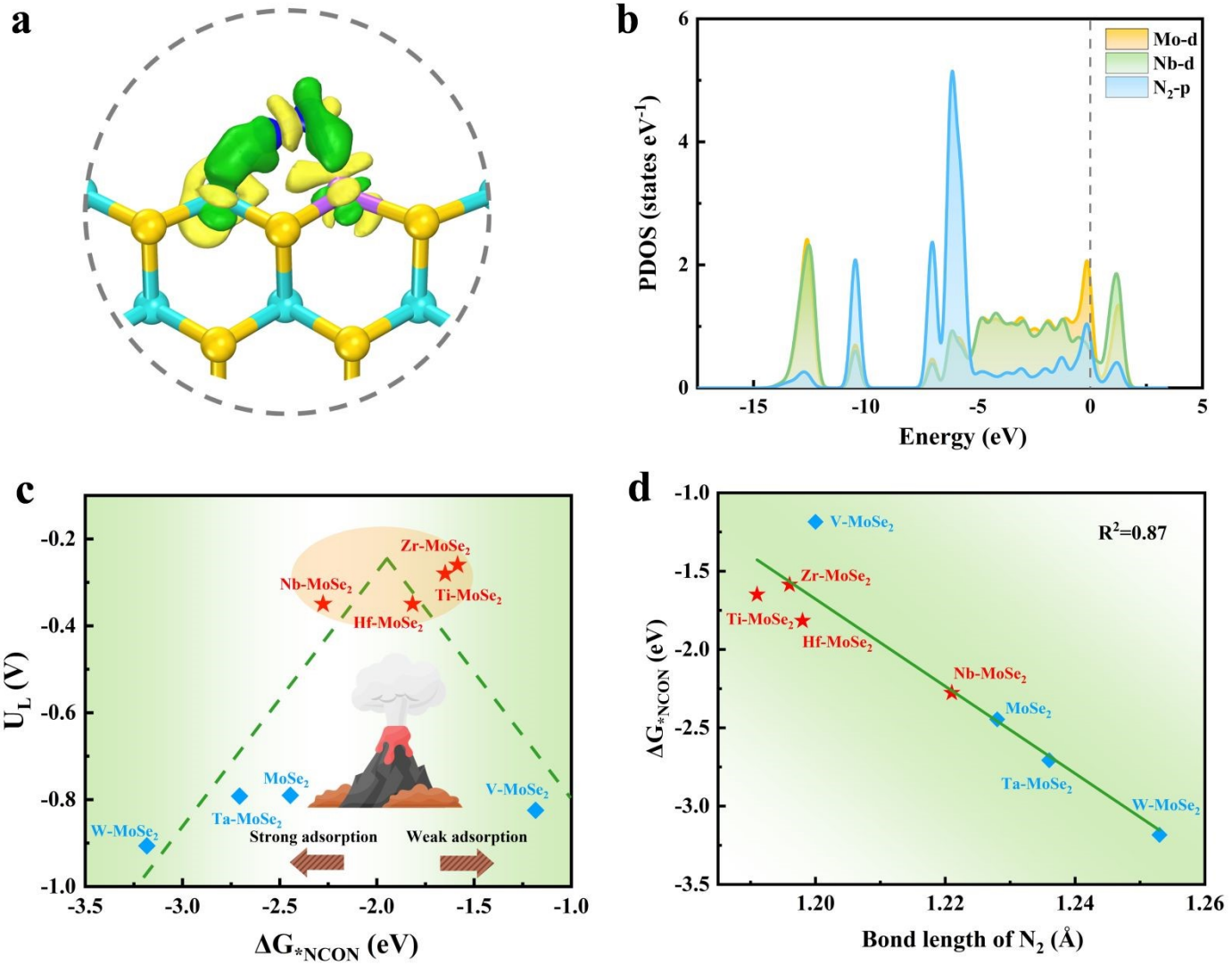

Fig.5 (a) The charge density difference of Nb-$MoSe_2$ with N_2 adsorption, where green (yellow) stands for the electron accumulation (depletion). (b) Projected density of states (PDOS) of $^*N_2$ adsorbed on Nb-$MoSe_2$. The Fermi level is set to 0 eV. (c) Volcano plot for the limiting potential of urea synthesis on eight systems as a function of ΔG_{*NCON}. (d) Linear scaling relationship between the bond length of $^*N_2$ and ΔG_{*NCON}. The catalysts with red asterisks are those whose limiting potentials meet the screening criteria.

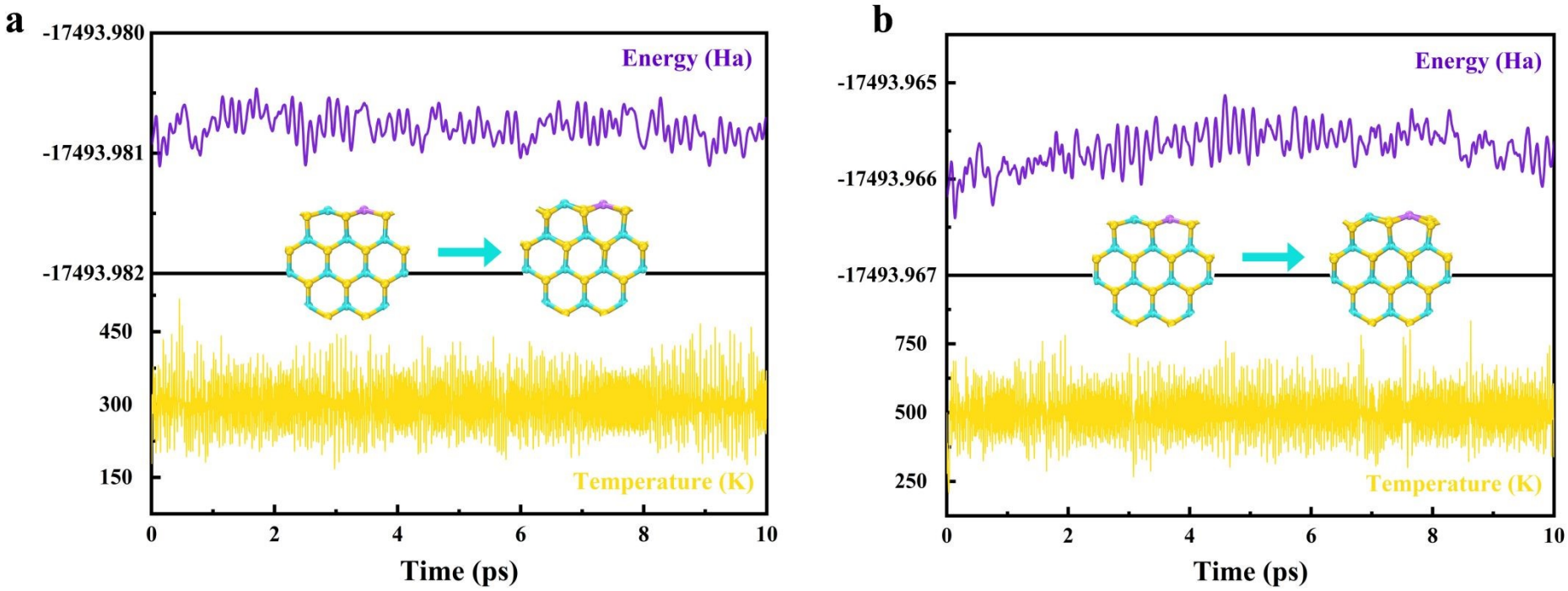

Fig. 6 AIMD simulations of Nb-$MoSe_2$ (a) at 300 K and (b) at 500 K.

View Article Online
DOI: 10.1039/D5TA04475H

Data Availability Statement

The data that supports the findings of this study are available on request from the corresponding author Dr Lianming Zhao upon reasonable request.